nanomaterials

MDPI

Article

Template-Free Preparation of α-Ni(OH)$_2$ Nanosphere as High-Performance Electrode Material for Advanced Supercapacitor

Rongrong Zhang [1,†], Qian Tu [1,†], Xianran Li [1], Xinyu Sun [1,*], Xinghai Liu [2,*] and Liangzhe Chen [1,*]

[1] School of Electronic Information Engineering, Jingchu University of Technology, Jingmen 448000, China; 200805001@jcut.edu.cn (R.Z.); tq010406@163.com (Q.T.); ggll925597@163.com (X.L.)
[2] Research Center of Graphic Communication, Printing and Packaging, Wuhan University, Wuhan 430079, China
* Correspondence: sxy007@jcut.edu.cn (X.S.); liuxh@whu.edu.cn (X.L); chen_lz1991@whu.edu.cn (L.C.)
† These authors contributed equally to this work.

Abstract: Although it is one of the promising candidates for pseudocapacitance materials, Ni(OH)$_2$ is confronted with poor specific capacitance and inferior cycling stability. The design and construction of three-dimensional (3D) nanosphere structures turns out to be a valid strategy to combat these disadvantages and has attracted tremendous attention. In this paper, a 3D α-Ni(OH)$_2$ nanosphere is prepared via a facile and template-free dynamic refluxing approach. Significantly, the α-Ni(OH)$_2$ nanosphere possesses a high specific surface area (119.4 m^2/g) and an abundant porous structure. In addition, the as-obtained α-Ni(OH)$_2$ electrodes are investigated by electrochemical measurements, which exhibit a high specific capacitance of 1243 F/g at 1 A/g in 6 M KOH electrolyte and an acceptable capacitive retention of 40.0% after 1500 charge/discharge cycles at 10 A/g, which can be attributed to the sphere's unique nanostructure. Furthermore, the as-assembled Ni(OH)$_2$-36//AC asymmetric supercapacitor (ASC) yields a remarkable energy density of 26.50 Wh/kg, with a power density of 0.82 kW/kg. Notably, two ASCs in series can light a 2.5 V red lamp sustainably for more than 60 min, as well as power an LED band with a rated power of 25 W. Hence, this 3D α-Ni(OH)$_2$ nanosphere may raise great potential applications for next-generation energy storage devices.

Keywords: α-Ni(OH)$_2$; nanosphere; supercapacitor; template-free; morphology engineering

Citation: Zhang, R.; Tu, Q.; Li, X.; Sun, X.; Liu, X.; Chen, L. Template-Free Preparation of α-Ni(OH)$_2$ Nanosphere as High-Performance Electrode Material for Advanced Supercapacitor. *Nanomaterials* **2022**, *12*, 2216. https://doi.org/10.3390/nano12132216

Academic Editor: Diego Cazorla-Amorós

Received: 26 May 2022
Accepted: 24 June 2022
Published: 28 June 2022

1. Introduction

The supercapacitor (SC), also known as an electrochemical capacitor, is deemed to be one of the most promising energy storage devices to address ever-increasing environmental issues and the energy crisis because of its the fast charge and discharge ability, high power density and long durability [1–5]. On the ground level of energy storage mechanisms, SCs are grouped into two categories: pseudocapacitance and electric double-layer capacitance (EDLC) [6,7]. As a common EDLC material, the activated carbon (AC) has tremendous applications owing to its low prices and abundant sources [8,9]. However, AC-based SCs suffer from poor specific capacitance and lower operating voltages (usually less than 1.0 V) [10,11]. Of the various strategies, the most effective candidate to remove these limitations is the fabrication of an asymmetric system, namely, the activated carbon and pseudocapacitance materials serve as negative and positive electrodes, respectively, which enables utilization of the advantages of two types of SCs. Hence, the primary task ahead is to focus on the study of positive electrode materials with excellent electrochemical performances [12,13].

In recent years, transition-metal hydroxide, especially Ni(OH)$_2$, has attracted intensive concerns as a result of its low cost, remarkable energy density and theoretical specific capacitance [14–16]. Even so, the shortcomings of inferior electric conductivity and poor

rate capability are becoming serious obstacles to the widespread application of supercapacitors [17–21]. Hence, more explorations are essential for coping with these limitations. Designing and constructing nanostructured $Ni(OH)_2$ materials turns out to be one of the most attractive strategies. Some researchers have pointed out that the excellent electrochemical properties of $Ni(OH)_2$-based electrodes rely on nanostructure morphology, which is associated with the preparation strategy. For instance, Sun et al. [22] synthesized few-layered $Ni(OH)_2$ nanosheets (4–5 nm in thickness), which show high specific capacitance and rate capacity in both electrode and supercapacitor. Niu et al. [23] prepared a unique ZnO nanofiber@$Ni(OH)_2$ core–shell heterostructure with a significant specific capacitance (of 2218 F/g at 2 mV/s). On the other hand, the nanostructure $Ni(OH)_2$ can create a larger specific surface area and supply more active sites, generating a shorter ion transfer pathway and higher capacitance [24]. In addition, since the topic of carbon neutrality has become prominent, designing and synthesizing a nanostructured $Ni(OH)_2$ in a simple, convenient and low-cost way is very meaningful.

More recently, Yang et al. [25] prepared a 3D MXene-based microsphere via the spray pyrolysis and selenization process, which exhibited an enhanced capacity and capacity retention. Inspired by this study, we design and propose a facile approach to fabricating a nanostructured α-$Ni(OH)_2$ nanosphere via a modified co-precipitation method without any template reagent, i.e., dynamic refluxing route. Compared with traditional methods, this present route is superior because of the simplified process (only one step) and freedom from high pressure (at normal pressure). It should be emphasized that the surface morphology and architecture can be easily controlled by adjusting the reaction times. Importantly, this 3D-nanostructured α-$Ni(OH)_2$ nanosphere displays a distinguished faradaic electrochemical performance with high specific capacitance and receptible cycling retention, which can be attributed to its large specific surface area and abundant mesoporous structure provided by the nanoball construction. Moreover, the assembled asymmetric supercapacitor ($Ni(OH)_2$-36//AC ASC) delivers remarkable power density and energy density, which is competitive with the $Ni(OH)_2$-based system in previous reports. Surprisingly, two ASCs in the series show good practical performances, which can not only light up a red lamp with a voltage of 2.5 V for more than 60 min, but also power an LED band with a rated power of 25 W. Hence, this paper proposes a facile approach for preparing the advanced electrode material for next-generation energy storage devices.

2. Materials and Methods

2.1. Materials and Chemicals

Nickel chloride ($NiCl_2 \cdot 6H_2O$), urea, acetone, ethanol, potassium hydroxide (KOH) and hydrochloric acid (HCl) were purchased from Shanghai Macklin Biochemical Co., Ltd. (Shanghai, China). All chemical reagents were of analytical purity and used without further processing. Nickel foam (1 mm in thickness) and polytetrafluoroethylene (PTFE) were received from Cyber Electro Chemical Materials. Acetylene black was obtained from Yilongsheng Energy Technology Co., Ltd. (Suzhou, China). and activated carbon (AC) (5 ± 1 μm in particle size, 1800 ± 100 m^2/g in specific surface area, 1.0–1.2 cm^3/g in pore volume and 0.38–0.40 g/cm^3 in tap density) was bought from Nanjing/Jiangsu XFNANO Materials Tech Co., Ltd. (Nanjing, China). The deionized water was used throughout the experiments.

2.2. Synthesis of the 3D α-Ni(OH)$_2$ Nanosphere

The α-$Ni(OH)_2$ nanosphere is synthesized via a facile dynamic reflux method. Briefly, 1.26 mmol of $NiCl_2 \cdot H_2O$ and 12.6 mmol of urea were dissolved in 50 mL of deionized water to obtain a homogeneous solution and were placed in a three-necked flask, which was heated at 105 °C for 24~60 h. Then, the filter cake was washed with deionized water until neutral and dried in a vacuum for another 24 h. According to the reaction time, the obtained $Ni(OH)_2$ compositions were labeled as $Ni(OH)_2$-24, $Ni(OH)_2$-36, $Ni(OH)_2$-48 and $Ni(OH)_2$-60, respectively.

2.3. Preparation of the α-Ni(OH)$_2$ Electrodes

The electrodes, including the α-Ni(OH)$_2$ electrode (anode) and AC electrode (cathode), were prepared by a screen-printing route, as shown in Figure S1. For screen-printed electrodes, an 80 wt% α-Ni(OH)$_2$ composite or AC, 10 wt% acetylene black and 10 wt% PTFE/ethanol emulsion were mixed by stirring continuously to form a homogeneous ink. Then, the resulting inks were forced through the screen plate (100 meshes) and printed on nickel foam with a square pattern of 1 cm × 1 cm, followed by drying at 80 °C for 3 h. Finally, the product was treated with pressure under 8 MPa for 1 min. Importantly, the loading mass of the electrode can be regulated by adjusting the printing times or ink concentration, and the loading mass of the working electrode was ~3.0 mg in this work.

2.4. Fabrication of the Asymmetrical Supercapacitor

The asymmetrical supercapacitor (ASC) was assembled on a Swagelok container with a "sandwich" structure. In general, the positive electrode, negative electrode and cellulose membrane were dipped into a 6 mol/L KOH solution for 5 min. Then, two electrodes were assembled face-to-face with a cellulose membrane between them. Finally, this "sandwich" was clamped by two stainless steel sheets under gentle pressure.

In order to obtain the best electrochemical performances, the mass ratios of Ni(OH)$_2$ and AC were designed via the charge–balance ($q^+ = q^-$) of the electrode materials according to equations [26,27]:

$$q = C_m \times \Delta V \times m \tag{1}$$

$$\frac{m^+}{m^-} = \frac{C^- \times \Delta V^-}{C^+ \times \Delta V^+} \tag{2}$$

where C_m, ΔV and m represent the specific capacitance of the positive and negative electrodes (F/g), potential windows (V) and the mass of active materials on positive and negative electrodes (g), respectively.

2.5. Fabrication of the Asymmetrical Supercapacitor

For the single electrode, the electrochemical performances were tested in a three-electrode cell with a 6 mol/L KOH electrolyte. The Ni(OH)$_2$ or AC electrode, Hg/HgO electrode and platinum plate served as the working electrode, reference electrode and counter electrode, respectively. For the asymmetrical supercapacitor (ASC), the electrochemical test was implemented in a two-electrode system, namely, the Ni(OH)$_2$ electrode and AC electrode served as the positive electrode and negative electrode, respectively. Then, cyclic voltammetry (CV), galvanostatic charge–discharge (GCD) and electrochemical impedance spectroscopy (EIS) and cycling stability test were measured at 25 °C. The energy density (E) and power density (P) of the ASC were calculated based on the following equations [28,29]:

$$\mathrm{E} = \frac{1}{2} C_m \Delta V^2 \tag{3}$$

$$\mathrm{P} = \frac{E}{t} \tag{4}$$

where C_m is the specific capacitance of the ASC based on the GCD curves (F/g), ΔV is the voltage window (V), and t is the discharge time (h).

2.6. Characterization

The phase structure of the samples was analyzed by an X-ray diffractometer (XRD, RIGAKU Miniflex600, Tokyo, Japan) with Cu Kα radiation (λ = 1.5406 Å) from 5 to 80°. The morphology was characterized by a scanning electron microscope (SEM, Zeiss SIGMA 500, Oberkochen, Germany) and a transmission electron microscope (TEM, FEI Tecnai G2 F20, Hillsboro, OR, USA) operated at 200 kV. The surface valence bond and functional group information were identified by X-ray photoelectron spectroscopy (XPS, ThermoFisher EscaLab250Xi, Waltham, MA, USA) with a monochromatic Al Kα radiation (1486.6 eV) and

Fourier transformed infrared spectrometer (FT-IR, ThermoFisher Nicolet 5700, Waltham, MA, USA) in the range of 500–4000 cm^{-1}. The specific surface area of the sample was studied by the Brunauer–Emmett–Teller method (BET, Micromeritics ASAP2000, Boynton Beach, FL, USA) at 77K. All electrochemical measurements were performed at a CS350H electrochemical workstation (CorrTest, Wuhan, China).

3. Results

3.1. Physical Characterization of the α-Ni(OH)$_2$ Nanosphere

The preparation procedure of the α-$Ni(OH)_2$ nanosphere by a facile co-precipitation route is schematically depicted in Figure S2. In general, the Ni^{2+} solution was added into the urea solution drop-by-drop under unceasing agitation. Then, the mixture was transferred to a round-bottom flask with a condenser pipe, followed by heating at 105 °C, and the 3D α-$Ni(OH)_2$ nanoball came into being after a while. Compared with the conventional routes for preparing spherical nanomaterials, it is worth noting that this one-step preparation process is free of both stirring and a template, which is conducive to large-scale production.

Figure 1a–d shows the surface morphology of the $Ni(OH)_2$ samples performed by SEM. It is evident that the $Ni(OH)_2$ nanoball is composed of interconnected and hierarchical nanoplates that have various diameters up to several micrometers. This spherical construction can provide an enlarged specific surface area for the interaction/reactions of ions, which is conducive to electron transfer, making it a desired electrode material for supercapacitors [30,31]. Notably, the globular structure changes as the reaction time increases. As seen in Figure 1a–d, the $Ni(OH)_2$-24 presents an incomplete globular structure, whereas $Ni(OH)_2$-36 displays an optimal morphology. However, the spherical structure gradually collapses and the nanosheets emerge as time goes on (Figure 1c,d), confirming the growth and dissolution process of the $Ni(OH)_2$ nanoball. In other words, the morphology of the $Ni(OH)_2$ nanosphere can be easily controlled by regulating the reaction time. In addition, TEM measurement was carried out to further confirm this unique structure. In Figure 1e, the nanostructure (2.3 μm in diameter) consists of ultrathin $Ni(OH)_2$ flakes, forming a globular structure, and several lattice fringes can be observed in the HRTEM image taken from the edge of the nanosphere (Figure 1f). Moreover, EDS mapping is utilized to identify the composition of the $Ni(OH)_2$ nanoball. Noticeably, the distributions of Zn and O elements, as well as C and N elements (originated from the urealysis) across the nanostructure, reveal the successful fabrication of the $Ni(OH)_2$ nanoball, and the mapping result is consistent with the EDS spectrum created in Figure S3.

In order to investigate the crystal structure of the as-prepared $Ni(OH)_2$ composites, the XRD patterns were recorded, and the results are presented in Figure S4. It is clear that all the samples have similar diffraction peaks, which can be indexed well to the rhombohedral phase of α-$Ni(OH)_2$ (Space group: *R*, JCPDS Card No. 38-0715) with lattice constants a = 3.08 Å and c = 8.00 Å [32]. The crystal-clear peaks at 2θ = 12.40, 24.90, 33.44 and 59.36° correspond to the lattice of the (003), (006), (101) and (110) planes, respectively. The intensive peak of the (003) plane reveals the high preferred (003) orientation. Note that no other impurity peaks are observed, demonstrating the high purity of the obtained α-$Ni(OH)_2$ [33]. However, the XRD reflection of the (003) and (006) planes are shifted towards high 2θ values, which may be due to the existence of the lattice distortion [34].

XPS measurement was utilized to analyze the chemical valence of the $Ni(OH)_2$-36 compound. As shown in Figure 2a, the XPS survey spectrum indicates the presence of Ni, O and N elements, which are consistent with the EDS mapping results. The deconvolution of the Ni 2p spectrum in Figure 2b displays two major peaks with satellite peaks (labelled as Sat.) centered at 873.3 and 855.6 eV, corresponding to the Ni $2p_{3/2}$ and Ni $2p_{1/2}$ spin–orbit levels, respectively, implying the +2 valence state of the Ni ions [35]. In addition, the observed spin–energy separation between Ni $2p_{3/2}$ and Ni $2p_{1/2}$ is ~17.7 eV, which is related to the characteristics of the $Ni(OH)_2$ phase [36]. The high resolution of the O 1s spectrum in Figure 2c can be divided into two components, including the nickel–oxygen bond at 531.2 eV and lattice oxygen at 528.6 eV, which is in line with previous reports [23,37].

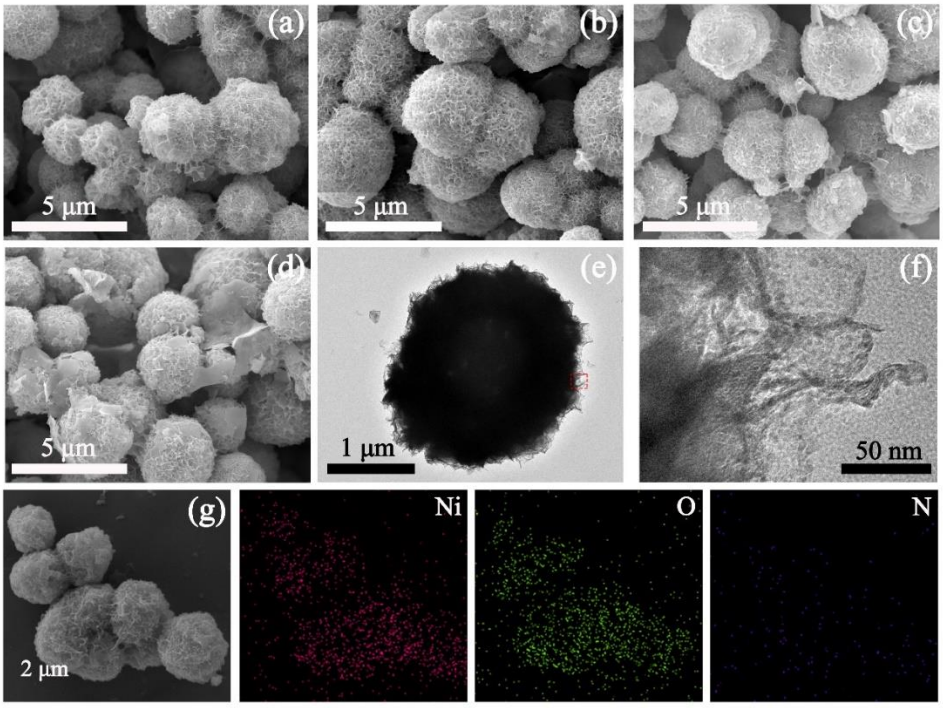

Figure 1. SEM images of (**a**) $Ni(OH)_2$-24; (**b**) $Ni(OH)_2$-36; (**c**) $Ni(OH)_2$-48; (**d**) $Ni(OH)_2$-60; (**e**) TEM image; (**f**) HRTEM image of $Ni(OH)_2$-36; (**g**) EDS mapping of $Ni(OH)_2$-36.

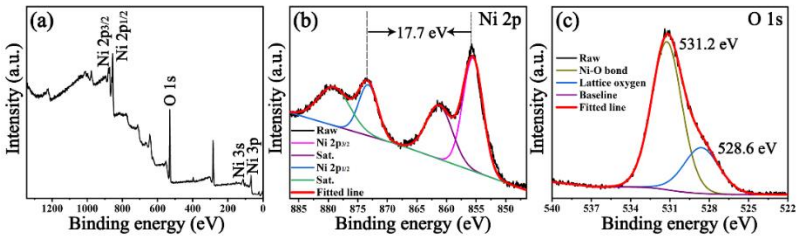

Figure 2. XPS spectra of (**a**) survey spectrum; high resolution of (**b**) Ni 2p and (**c**) O 1s for $Ni(OH)_2$-36.

The functional group information of the composites was investigated by FT-IR spectra. It is clear in Figure S5 that similar peaks can be found in all $Ni(OH)_2$ samples. The weak peak at 635 cm^{-1} is assigned to the Ni-O bending vibration, confirming the successful preparation of $Ni(OH)_2$ [38]. The peak at ~1390 cm^{-1} is attributed to the C-O stretching vibration, indicating the intercalation of carbonate anions in the interlamination due to the dissociation of the urea [23,39]. In addition, two bands at 3445 and 1630 cm^{-1} are related to the O-H vibration from the hydroxyl groups or adsorbed water molecules of $Ni(OH)_2$.

According to the above measurements, the formation process of the $Ni(OH)_2$ nanosphere is proposed in Figure 3. Firstly, $CO(NH_2)_2$ releases hydroxyl ions at a high temperature, giving rise to the formation of a $Ni(OH)_2$ crystal nucleus, and the corresponding reactions are suggested as follows [40–42]:

$$CO(NH_2)_2 + H_2O \rightarrow CO_2 + 2NH_3 \quad (5)$$

$$NH_3 + H_2O \rightarrow NH_4^+ + OH^- \quad (6)$$

$$Ni^{2+} + 2OH^- \rightarrow \alpha Ni(OH)_2 \quad (7)$$

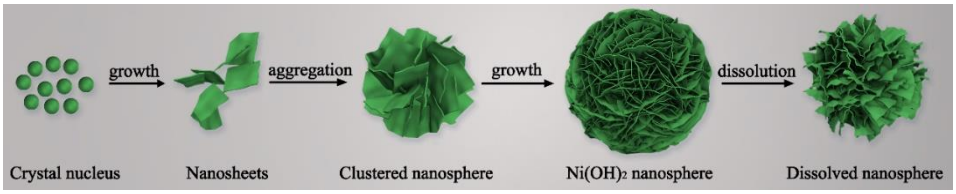

Figure 3. The formation mechanism of the 3D α-$Ni(OH)_2$ nanosphere.

Crystal nuclei in the solution gather to lower interfacial energy, and nanoflakes are formed due to the fast growth velocity of the (003) lattice plane. Owing to the intermolecular hydrogen bonds, the nanoflakes agglomerate and therefore generate the spherical structure to lower energy. Then, the nanosphere grows up with larger and thinner nanoplates. It is noteworthy that the nanoball will be dissolved by excess hydroxyl ions, bringing about the collapse of the spheroidal architecture (as shown in Figure 1a–d).

3.2. Electrochemical Performances

The electrochemical characterizations of as-prepared samples were conducted by CV, GCD, EIS and cycling performance in a three-electrode configuration. Figure 4a shows the typical CV curves at a scan rate of 10 mV/s in the potential window of 0 to 0.55 V. Unambiguously, a pair of redox peaks can be observed in all the electrodes, suggesting the characteristic faradic reaction derived from $Ni(OH)_2$, and the corresponding redox reaction is as follows [43]:

$$Ni(OH)_2 + OH^- \leftrightarrow NiOOH + H_2O + e^- \quad (8)$$

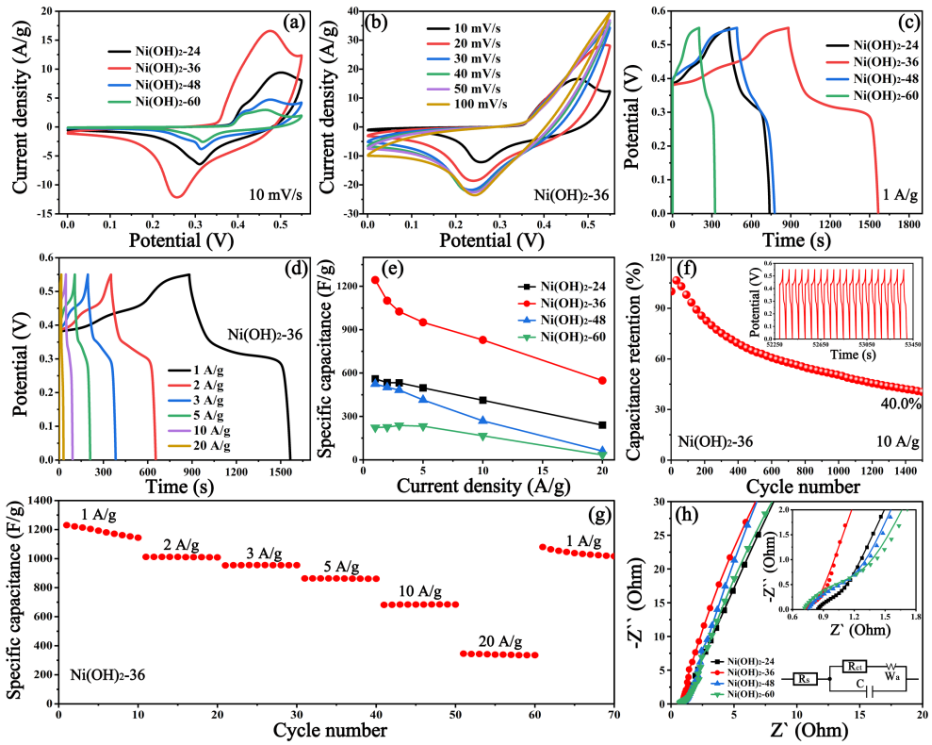

Figure 4. (**a**) CV curves of different samples at 10 mV/s; (**b**) CV curves of $Ni(OH)_2$-36 electrode at various scan rates; (**c**) GCD curves of different samples at 1 A/g; (**d**) GCD curves of $Ni(OH)_2$-36 electrode at different current densities; (**e**) obtained specific capacitance of different electrodes at various current densities; (**f**) cycling stability of $Ni(OH)_2$-36 at 10 A/g after 1500 cycles, the inset shows the last 20 cycles; (**g**) rate performance of $Ni(OH)_2$-36 at different current density; (**h**) Nyquist plots of the prepared electrodes, the illustrations on the upper and lower right display the enlarged Nyquist plots in the high-frequency region and equivalent circuit respectively.

In contrast with other samples, the integral area of the CV curve for $Ni(OH)_2$-36 is much higher, suggesting the prominently enhanced specific capacitance. Further, the CV curves with stable shapes of different samples at various scan rates reveal the good faradaic pseudocapacitance of the $Ni(OH)_2$ samples (Figures 4b and S6). Figure 4b supports the result of the CV curve, in which the $Ni(OH)_2$-36 electrode has a longer discharge time than other electrodes, demonstrating a better specific capacitance. Figures 4d and S7 display the GCD curves of all electrodes at different current densities. It was found that a complete charging and discharging process can be implemented even at a high current density, implying the good reversibility of the redox process [44]. The voltage platforms in the charge/discharge process indicate the existence of Faradic redox reactions. The mass-specific capacitance (C_m) can be calculated using the following equation [45]:

$$C_m = \frac{I \times \Delta t}{m \times \Delta V} \quad (9)$$

where I is the discharge current (A), m is the mass of the active materials in the electrode (g), Δt is the discharge time (s), and ΔV is the potential window (V).

According to Equation (9), the results of the calculation for the C_m are represented in Figure 4e. It is expected that the C_m of $Ni(OH)_2$-36 (1243 F/g) at 1 A/g is much higher compared with the $Ni(OH)_2$-24 (560 F/g), $Ni(OH)_2$-48 (524 F/g) and $Ni(OH)_2$-60 (223 F/g) electrodes, exhibiting the excellent electrochemical performance of $Ni(OH)_2$-36. Compared with single $Ni(OH)_2$-based materials from previous reports (Table S1), this specific capacitance value is competitive, even better than some $Ni(OH)_2$-based composites. Further, the capacitance retention of $Ni(OH)_2$-36 at 20 A/g is up to 44.07%, which is greater than $Ni(OH)_2$-24 (42.86%), $Ni(OH)_2$-48 (11.55%) and $Ni(OH)_2$-60 (15.17%). The enhanced specific capacitance of $Ni(OH)_2$-36 is probably due to the specific area resulting from the ball texture, which is verified by the N_2 adsorption/desorption isotherms in Figure S8 and Table S2. The average pore sizes of all samples range from 3.401 to 3.807 nm and can be considered mesoporous materials [46]. Remarkably, the $Ni(OH)_2$-36 exhibits a larger BET-specific surface area of 119.4 m^2/g than $Ni(OH)_2$-24 (42.0 m^2/g), $Ni(OH)_2$-48 (59.2 m^2/g) and $Ni(OH)_2$-60 (37.1 m^2/g). A larger specific surface area of $Ni(OH)_2$-36 can provide more active sites and motivate the diffusion of ions into inner materials, which will lead to higher capacitance [47].

Figure 4f depicts the cycling stability of $Ni(OH)_2$-36 at 10 A/g after 1500 cycles with a potential of 0–0.55 V. A low capacitance retention of 40.0% is observed the in $Ni(OH)_2$-36 electrode after 1500 continuous charge and discharge cycles; the reason for this is the poor conductivity of the nickel hydroxide itself. The rate performance has been investigated by GCD measurement. As shown in Figure 4g, the $Ni(OH)_2$-36 electrode experiences 10 consecutive cycles at various current densities (1, 2, 3, 5, 10 and 20 A/g), then comes back to 1 A/g to run another 10 cycles. Advantageously, the specific capacitance $Ni(OH)_2$-36 electrode declines with the increase in current densities and returns closed to its original level when the current density increases to 1 A/g, indicating good rate cycling behavior. Moreover, the electrochemical dynamics are revealed by EIS measurement, as illustrated in Figure 4h. In the Nyquist plots, a semicircle (in the high-frequency region) and linear part (in the low-frequency region) are observed in all curves. The equivalent circuit model is illustrated in the inset, as are the components of *Rs* (electrolyte resistance), *C* (Faradaic capacitance), *Rct* (charge transfer resistance) and *Wa* (Warburg resistance). According to the equivalent circuit, the corresponding parameters are listed in Table S3. A smaller *Rct* value of 0.35 Ω is obtained from $Ni(OH)_2$-36 compared with those of $Ni(OH)_2$-24 (0.48 Ω), $Ni(OH)_2$-48 (0.89 Ω) and $Ni(OH)_2$-60 (0.99 Ω), proving the faster charge transfer of $Ni(OH)_2$-36 due to the large surface area.

With the aim of examining the merits of $Ni(OH)_2$-36 in the energy storage device, the $Ni(OH)_2$-36//AC asymmetrical supercapacitor, which is composed of a positive electrode ($Ni(OH)_2$-36), a negative electrode (AC), separator and electrolyte (6M KOH), is assembled in a Swagelok cell with a "sandwich" structure, and the corresponding configuration is

diagramed in Figure 5a. For an asymmetrical supercapacitor device, the mass ratio of the electrodes is vital, which can be determined by the principle of charge balance according to Equations (1) and (2). Figure 5b displays the CV curves of AC, with a potential of −1.1–0 V, and $Ni(OH)_2$-36, with a potential of 0–0.55 V. The specific capacitance (C_m) is calculated from the CV curves by the following equation [34]:

$$C_m = \frac{\int I(V)dV}{m \times v \times \Delta V} \tag{10}$$

where $\int I(V)dV$ is the enclosed areas, m is the mass of active materials, and ΔV is the potential window, respectively. Based on Equation (10), the obtained C_m of AC and $Ni(OH)_2$-36 at 10 mV/s are 158.62 and 437.07 F/g, respectively, and the mass ratio of AC to $Ni(OH)_2$-36 is suggested to be ~2.8 in the ASC. In addition, there are no explicit polarization curves in both samples, indicating an ideal capacitive behavior with a total potential window of 1.65 V.

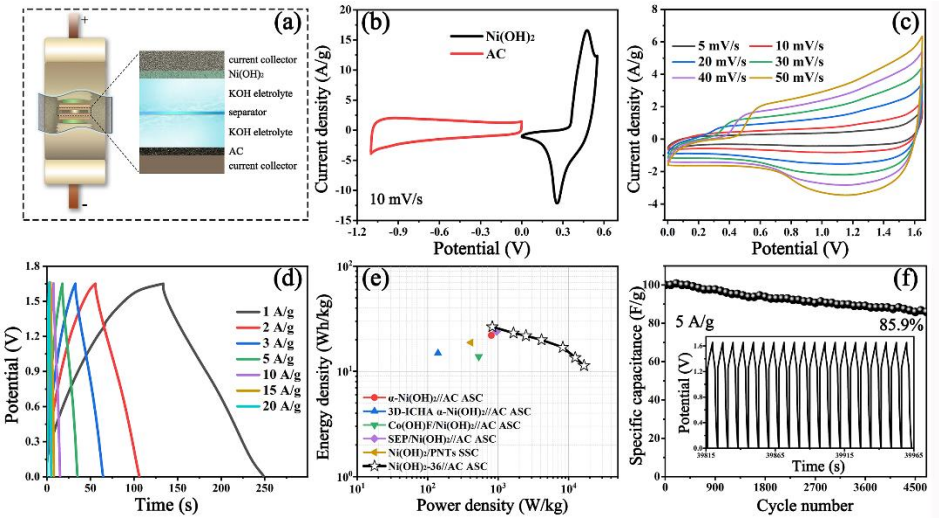

Figure 5. (**a**) Diagram of the as-prepared $Ni(OH)_2$-36//AC ASC; (**b**) CV curves of the $Ni(OH)_2$-36 and AC electrodes at 10 mV/s; (**c**) CV curves of the ASC at various scan rates; (**d**) GCD curves of the ASC at various current densities; (**e**) Ragone plots of the $Ni(OH)_2$-36//AC ASC in contrast with other $Ni(OH)_2$-based supercapacitor reported in previous reports; (**f**) cycling performance of the $Ni(OH)_2$-36//AC ASC at 5 A/g (the inset shows the last 20 cycles).

The CV curves ranging from 5 to 50 mV/s in Figure 5c reveal that the as-prepared $Ni(OH)_2$-36//AC ASC represents common contributions of both EDLC and pseudocapacitance, and the shape of the curve is maintained evenly at 50 mV/s, implying good reversibility. Figure 5d shows the GCD curves at various current densities, and the C_m are calculated as 70.1, 61.2, 57.7, 52.7, 44.8, 35.8 and 30.0 F/g at 1, 2, 3, 5, 10, 15 and 20 A/g, respectively. According to Equations (3) and (4), the Ragone plots of the as-obtained $Ni(OH)_2$-36//AC ASC are given in Figure 5e, and the details can be found in Table 1. It was observed that a maximum energy density of 26.50 Wh/kg can be achieved with a power density of 0.82 kW/kg, and a maximum power density can reach up to 16.50 kW/kg, whereas the energy density still maintains 11.34 Wh/kg, confirming the outstanding rate performance of our $Ni(OH)_2$-36//AC ASC. Impressively, these results outperform those of a $Ni(OH)_2$-based supercapacitor, such as α-$Ni(OH)_2$ nanosheet//AC (22.00 Wh/kg at 0.80 kW/kg) [24], 3D-ICHA α-$Ni(OH)_2$//AC (14.86 Wh/kg at 0.14 kW/kg) [11], $Co(OH)F/Ni(OH)_2$//AC (13.80 Wh/kg at 0.53 kW/kg) [42], $SEP/Ni(OH)_2$//AC (24.00 Wh/kg at 0.95 kW/kg) [22] and $Ni(OH)_2$/PNTs//$Ni(OH)_2$/PNTs (18.80 Wh/kg at 0.41 kW/kg) [48]. Figure 5f shows the cycling performance of the ASC. It is emphasized that a slight increase in the C_m before 200 cycles is probably due to the augmentation of electrochemically active sites, and a

steady level is retained in the following cycles. After 4700 continual cycles at 5 A/g, this ASC device still has a remarkable capacitance retention of 85.9%, revealing the high electrochemical stability that can allow it to act as an energy storage device. Furthermore, Nyquist plots of the $Ni(OH)_2$-36//AC ASC before and after cycles are created in Figure S9 and Table S4. The *Rct* value before the cycles decreases to 3.38 Ω, showing notable conductivity and fast ion diffusion. However, it grows to 27.08 Ω after 4700 cycles, resulting in the decline of specific capacitance.

Table 1. Performance comparison of $Ni(OH)_2$-based supercapacitors from previous reports.

Supercapacitors	ΔV(V)	Conditions	C_m(F/g)	P(W/kg)	E(Wh/kg)	Ref.
$Ni(OH)_2$-36//AC	1.65	1 A/g	70	825	26.5	This work
α-$Ni(OH)_2$//AC	1.60	1 A/g	248	800	22.0	[22]
3D-ICHA α-$Ni(OH)_2$//AC	1.55	1.04 A/g	50.7	140	14.9	[11]
Co(OH)F/$Ni(OH)_2$//AC	1.50	0.5 A/g	45	530	13.8	[42]
SEP/$Ni(OH)_2$//AC	1.9	1.0 A/g	-	950	24.0	[48]
$Ni(OH)_2$/PNTs	0.8	1.0 A/g	212	410	18.8	[49]

For the purpose of investigating practical applications, two $Ni(OH)_2$-36//AC ASCs were assembled in series to light up a red lamp (2.5 V), as presented in Figure 6a. Note that the small lamp gives off light even after 60 min. Furthermore, as displayed in Figure 6b, a flexible LED lamp band with a Bluetooth controller (the output rated power of 25 W) was powered by two SSCs in a series, and the word "JCUT" was shown for a few seconds, fully proving the large potential application of the energy device.

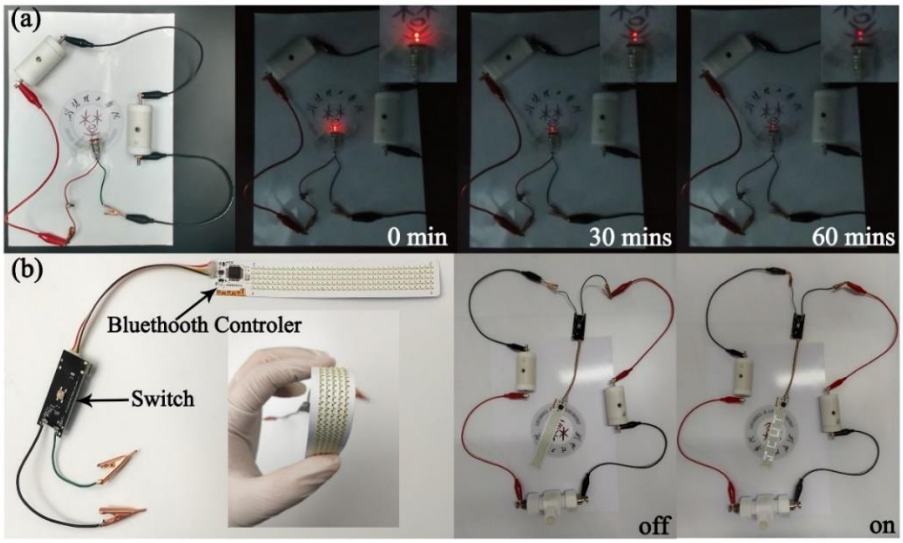

Figure 6. (**a**) Digital photograph of lighting the red lamp (2.5V) powered by two SSCs in series for more than 60 min; (**b**) photo of the flexible LED lamp band that was powered by three SSCs in series.

4. Conclusions

In summary, we have put forward a facile strategy for the preparation of a 3D α-$Ni(OH)_2$ nanosphere without any template agents as a high-performance electrode material for advanced supercapacitors. By making full use of this spherical architecture, the α-$Ni(OH)_2$ nanosphere represents a high specific capacitance of 1243.3 F/g at 1 A/g with an excellent rate of performance, as well as acceptable cycling stability after 1500 cycles at a large current density. We supposed that the enhanced electrochemical performance results from the unique morphology of the 3D nanosphere structure, which enables the supply of a large surface area and improves the diffusion and migration of ions in the electrochemical process. Moreover, the assembled $Ni(OH)_2$-36//AC ASC shows an outstanding

cycling stability of 84.7% after 4700 cycles, and it yields an impressive energy density of 26.50 Wh/kg with a power density of 0.82 kW/kg, which slightly outperforms the reported $Ni(OH)_2$-based supercapacitors. Subsequently, practical applications are further investigated. Surprisingly, two ASCs in series can light a 2.5 V red lamp for more than 60 min, and an LED band with a rated power of 25 W can be powered successfully. In consideration of the facile and low-cost preparation and the remarkable electrochemical properties, the 3D α-$Ni(OH)_2$ nanospheres may hold great potential applications for supercapacitors. More importantly, this facile strategy can be a reference for the fabrication of other spherical nanomaterials for next-generation energy storage materials.

Supplementary Materials: The following supporting information can be downloaded at: https://www.mdpi.com/article/10.3390/nano12132216/s1, Figure S1: Diagram of the preparation of the screen-printed electrodes; Figure S2: Schematic illustration for the preparation of the Ni(OH)2 nanospheres; Figure S3: EDS spectrum of the Ni(OH)2 nanospheres; Figure S4: XRD patterns of Ni(OH)2-24, Ni(OH)2-36, Ni(OH)2-48 and Ni(OH)2-60; Figure S5: FT-IR spectra of Ni(OH)2-24, Ni(OH)2-36, Ni(OH)2-48 and Ni(OH)2-60; Figure S6: CV curves of Ni(OH)2-24, Ni(OH)2-48 and Ni(OH)2-60 electrodes.; Figure S7: GCD curves of Ni(OH)2-24, Ni(OH)2-48 and Ni(OH)2-60 electrodes; Figure S8: N2 adsorption/desorption isotherm plots and the corresponding pore size distribution of Ni(OH)2-24, Ni(OH)2-36, Ni(OH)2-48 and Ni(OH)2-60; Figure S9: Nyquist plots of the Ni(OH)2-36//AC ASC before and after cycles (the inset show the enlarge high-frequency region of the plot and the equivalent circuit); Table S1: Specific capacitance comparison of Ni(OH)2-based materials from literature reports [22,50–58]; Table S2: Specific surface area, total pore volume and average pore size parameters for Ni(OH)2-24, Ni(OH)2-36, Ni(OH)2-48 and Ni(OH)2-60; Table S3: The EIS parameters of Rs, Rct, Wa and *C* for $Ni(OH)_2$-24, $Ni(OH)_2$-36, $Ni(OH)_2$-48 and $Ni(OH)_2$-60 electrodes; Table S4: The EIS parameters of *Rs*, *Rct*, *Wa* and *C* for the $Ni(OH)_2$-36//AC ASC before and after cycles.

Author Contributions: Conceptualization, L.C.; methodology, Q.T.; software, Q.T. and X.L. (Xianran Li); validation, L.C.; formal analysis, R.Z.; investigation, Q.T.; resources, R.Z.; data curation, X.L. (Xianran Li); writing—original draft preparation, Q.T. and L.C.; writing—review and editing, L.C.; supervision, R.Z., X.L. (Xinghai Liu) and L.C.; project administration, L.C.; funding acquisition, R.Z., X.S. and L.C. All authors have read and agreed to the published version of the manuscript.

Funding: This work was supported by the Natural Science Foundation of Hubei Province (2021CFB215), the Jingmen Science and Technology Project (2021YFYB119), the Scientific Project of Jingchu University of Technology (YB201807), the Scientific Research Team of Jingchu University of Technology (TD202101) and the Innovation and Entrepreneurship Training Program for College Students (KC2022022).

Institutional Review Board Statement: Not applicable.

Informed Consent Statement: Not applicable.

Data Availability Statement: Not applicable.

Conflicts of Interest: The authors declare no conflict of interest.

References

1. Li, K.; Li, J.; Zhu, Q.; Xu, B. Three-Dimensional MXenes for Supercapacitors: A Review. *Small Methods* **2022**, *6*, 2101537. [CrossRef] [PubMed]
2. Li, Q.; Liu, M.; Huang, F.; Zuo, X.; Wei, X.; Li, S.; Zhang, H. Co_9S_8@MnO_2 core–shell defective heterostructure for High-Voltage flexible supercapacitor and Zn-ion hybrid supercapacitor. *Chem. Eng. J.* **2022**, *437*, 135494. [CrossRef]
3. Qin, H.; Liu, P.; Chen, C.; Cong, H.-P.; Yu, S.-H. A multi-responsive healable supercapacitor. *Nat. Commun.* **2021**, *12*, 4297. [CrossRef] [PubMed]
4. Liang, R.; Du, Y.; Xiao, P.; Cheng, J.; Yuan, S.; Chen, Y.; Yuan, J.; Chen, J. Transition Metal Oxide Electrode Materials for Supercapacitors: A Review of Recent Developments. *Nanomaterials* **2021**, *11*, 1248. [CrossRef]
5. Niu, L.; Wu, T.; Chen, M.; Yang, L.; Yang, J.; Wang, Z.; Kornyshev, A.A.; Jiang, H.; Bi, S.; Feng, G. Conductive Metal-Organic Frameworks for Supercapacitors. *Adv. Mater.* **2022**, e2200999. [CrossRef]
6. Xie, P.; Yuan, W.; Liu, X.; Peng, Y.; Yin, Y.; Li, Y.; Wu, Z. Advanced carbon nanomaterials for state-of-the-art flexible supercapacitors. *Energy Storage Mater.* **2021**, *36*, 56–76. [CrossRef]

7. Lobato, B.; Suárez, L.; Guardia, L.; Centeno, T.A. Capacitance and surface of carbons in supercapacitors. *Carbon* **2017**, *122*, 434–445. [CrossRef]
8. Zhang, X.; Wang, Y.; Yu, X.; Tu, J.; Ruan, D.; Qiao, Z. High-performance discarded separator-based activated carbon for the application of supercapacitors. *J. Energy Storage* **2021**, *44*, 103378. [CrossRef]
9. Wang, C.; Wang, J.; Wu, W.; Qian, J.; Song, S.; Yue, Z. Feasibility of activated carbon derived from anaerobic digester residues for supercapacitors. *J. Power Sources* **2019**, *412*, 683–688. [CrossRef]
10. Brousse, T.; Bélanger, D.; Long, J.W. To be or not to be pseudocapacitive? *J. Electrochem. Soc.* **2015**, *162*, A5185. [CrossRef]
11. Gu, C.; Ge, X.; Wang, X.; Tu, J. Cation–anion double hydrolysis derived layered single metal hydroxide superstructures for boosted supercapacitive energy storage. *J. Mater. Chem. A* **2015**, *3*, 14228–14238. [CrossRef]
12. Chhetri, K.; Tiwari, A.P.; Dahal, B.; Ojha, G.P.; Mukhiya, T.; Lee, M.; Kim, T.; Chae, S.; Muthurasu, A.; Kim, H.Y. A ZIF-8-derived nanoporous carbon nanocomposite wrapped with Co_3O_4-polyaniline as an efficient electrode material for an asymmetric supercapacitor. *J. Electroanal. Chem.* **2020**, *856*, 113670. [CrossRef]
13. Chhetri, K.; Dahal, B.; Mukhiya, T.; Tiwari, A.P.; Muthurasu, A.; Kim, H.Y. Integrated hybrid of graphitic carbon-encapsulated Cu_xO on multilayered mesoporous carbon from copper MOFs and polyaniline for asymmetric supercapacitor and oxygen reduction reactions. *Carbon* **2021**, *179*, 89–99. [CrossRef]
14. Yang, Y.; Wang, X.; Huang, F.; Zhao, J.; Wang, X. $Ni(OH)_2$ nanodot-decorated Co-Co LDH/C hollow nanocages for a high performance supercapacitor. *Dalton Trans.* **2020**, *49*, 17310–17320. [CrossRef]
15. Zhang, J.; Wang, Z.; Deng, T.; Zhang, W. $Ni(OH)_2$ derived Ni-MOF supported on carbon nanowalls for supercapacitors. *Nanotechnology* **2021**, *32*, 195404. [CrossRef]
16. Xin, Y.; Dai, X.; Lv, G.; Wei, X.; Li, S.; Li, Z.; Xue, T.; Shi, M.; Zou, K.; Chen, Y.; et al. Stability-Enhanced α-$Ni(OH)_2$ Pillared by Metaborate Anions for Pseudocapacitors. *ACS Appl. Mater. Interf.* **2021**, *13*, 28118–28128. [CrossRef]
17. Yu, D.; Zheng, X.; Chen, M.; Dong, X. Large-scale synthesis of $Ni(OH)_2$/peach gum derived carbon nanosheet composites with high energy and power density for battery-type supercapacitor. *J. Colloid Inter. Sci.* **2019**, *557*, 608–616. [CrossRef]
18. Ma, L.; Kang, C.; Fu, L.; Cao, S.; Zhu, H.; Liu, Q. Core-shell $Ni_{1.5}Sn$@$Ni(OH)_2$ nanoflowers as battery-type supercapacitor electrodes with high rate and capacitance. *J. Colloid Interf. Sci.* **2022**, *613*, 244–255. [CrossRef]
19. Yuan, Y.; Jia, H.; Liu, Z.; Wang, L.; Sheng, J.; Fei, W. A highly conductive $Ni(OH)_2$ nano-sheet wrapped $CuCo_2S_4$ nano-tube electrode with a core-shell structure for high performance supercapacitors. *Dalton Trans.* **2021**, *50*, 8476–8486. [CrossRef]
20. Shi, X.; Key, J.; Ji, S.; Linkov, V.; Liu, F.; Wang, H.; Gai, H.; Wang, R. $Ni(OH)_2$ Nanoflakes Supported on 3D Ni_3Se_2 Nanowire Array as Highly Efficient Electrodes for Asymmetric Supercapacitor and Ni/MH Battery. *Small* **2019**, *15*, e1802861. [CrossRef]
21. Dong, B.; Li, M.; Chen, S.; Ding, D.; Wei, W.; Gao, G.; Ding, S. Formation of g-C_3N_4@$Ni(OH)_2$ Honeycomb Nanostructure and Asymmetric Supercapacitor with High Energy and Power Density. *ACS Appl. Mater. Interf.* **2017**, *9*, 17890–17896. [CrossRef] [PubMed]
22. Sun, W.; Rui, X.; Ulaganathan, M.; Madhavi, S.; Yan, Q. Few-layered $Ni(OH)_2$ nanosheets for high-performance supercapacitors. *J. Power Sources* **2015**, *295*, 323–328. [CrossRef]
23. Niu, H.; Zhou, D.; Yang, X.; Li, X.; Wang, Q.; Qu, F. Towards three-dimensional hierarchical ZnO nanofiber@$Ni(OH)_2$ nanoflake core–shell heterostructures for high-performance asymmetric supercapacitors. *J. Mater. Chem. A* **2015**, *3*, 18413–18421. [CrossRef]
24. Ji, J.; Zhang, L.L.; Ji, H.; Li, Y.; Zhao, X.; Bai, X.; Fan, X.; Zhang, F.; Ruoff, R.S. Nanoporous $Ni(OH)_2$ thin film on 3D Ultrathin-graphite foam for asymmetric supercapacitor. *ACS Nano* **2013**, *7*, 6237–6243. [CrossRef]
25. Yang, S.H.; Lee, Y.J.; Kang, H.; Park, S.K.; Kang, Y.C. Carbon-Coated Three-Dimensional MXene/Iron Selenide Ball with Core-Shell Structure for High-Performance Potassium-Ion Batteries. *Nano Micro Lett.* **2021**, *14*, 17. [CrossRef]
26. Wang, F.; Liu, X.; Chen, F.; Wan, H.; Lin, Y.; Zhang, N.; Ma, R. Advanced supercapacitors based on α-$Ni(OH)_2$ nanoplates/graphene composite electrodes with high energy and power density. *ACS Appl. Energy Mater.* **2018**, *1*, 1496–1505. [CrossRef]
27. Ji, Z.; Li, N.; Zhang, Y.; Xie, M.; Shen, X.; Chen, L.; Xu, K.; Zhu, G. Nitrogen-doped carbon dots decorated ultrathin nickel hydroxide nanosheets for high-performance hybrid supercapacitor. *J. Colloid Interf. Sci.* **2019**, *542*, 392–399. [CrossRef]
28. Zheng, S.; Wang, H.; Das, P.; Zhang, Y.; Cao, Y.; Ma, J.; Liu, S.F.; Wu, Z.S. Multitasking MXene Inks Enable High-Performance Printable Microelectrochemical Energy Storage Devices for All-Flexible Self-Powered Integrated Systems. *Adv. Mater.* **2021**, *33*, e2005449. [CrossRef]
29. Zhou, Y.; Li, J.; Hu, S.; Qian, G.; Shi, J.; Zhao, S.; Wang, Y.; Wang, C.; Lian, J. Sawdust-Derived Activated Carbon with Hierarchical Pores for High-Performance Symmetric Supercapacitors. *Nanomaterials* **2022**, *12*, 810. [CrossRef]
30. Qiao, S.; Huang, N.; Sun, Y.; Zhang, J.; Zhang, Y.; Gao, Z. Microwave-assisted synthesis of novel 3D flower-like $NiMnO_3$ nanoballs as electrode material for high-performance supercapacitors. *J. Alloy Compd.* **2019**, *775*, 1109–1116. [CrossRef]
31. Tseng, C.A.; Sahoo, P.K.; Lee, C.P.; Lin, Y.T.; Xu, J.H.; Chen, Y.T. Synthesis of CoO-Decorated Graphene Hollow Nanoballs for High-Performance Flexible Supercapacitors. *ACS Appl. Mater. Interf.* **2020**, *12*, 40426–40432. [CrossRef] [PubMed]
32. Zhang, J.; Liu, S.; Pan, G.; Li, G.; Gao, X. A 3D hierarchical porous α-$Ni(OH)_2$/graphite nanosheet composite as an electrode material for supercapacitors. *J. Mater. Chem. A* **2014**, *2*, 1524–1529. [CrossRef]
33. Chai, H.; Peng, X.; Liu, T.; Su, X.; Jia, D.; Zhou, W. High-performance supercapacitors based on conductive graphene combined with $Ni(OH)_2$ nanoflakes. *RSC Adv.* **2017**, *7*, 36617–36622. [CrossRef]

34. Lin, T.; Wang, L.; Wang, X.; Zhang, Y.; Yu, Y. Influence of lattice distortion on phase transition properties of polycrystalline VO_2 thin film. *Appl. Surf. Sci.* **2016**, *379*, 179–185. [CrossRef]
35. Hong, Y.; Xu, J.; Chung, J.S.; Choi, W. Graphene quantum dots/$Ni(OH)_2$ nanocomposites on carbon cloth as a binder-free electrode for supercapacitors. *J. Mater. Sci. Technol.* **2020**, *58*, 73–79. [CrossRef]
36. Jiang, C.; Zhao, B.; Cheng, J.; Li, J.; Zhang, H.; Tang, Z.; Yang, J. Hydrothermal synthesis of $Ni(OH)_2$ nanoflakes on 3D graphene foam for high-performance supercapacitors. *Electrochim. Acta* **2015**, *173*, 399–407. [CrossRef]
37. Tian, J.; Shan, Q.; Yin, X.; Wu, W. A facile preparation of graphene/reduced graphene oxide/$Ni(OH)_2$ two dimension nanocomposites for high performance supercapacitors. *Adv. Powder Technol.* **2019**, *30*, 3118–3126. [CrossRef]
38. Li, B.; Cao, H. ZnO@graphene composite with enhanced performance for the removal of dye from water. *J. Mater. Chem.* **2011**, *21*, 3346–3349. [CrossRef]
39. Nivangune, N.T.; Ranade, V.V.; Kelkar, A.A. MgFeCe ternary layered double hydroxide as highly efficient and recyclable heterogeneous base catalyst for synthesis of dimethyl carbonate by transesterification. *Catal. Lett.* **2017**, *147*, 2558–2569. [CrossRef]
40. Chuo, H.; Gao, H.; Yang, Q.; Zhang, N.; Bu, W.; Zhang, X. Rationally designed hierarchical $ZnCo_2O_4$/Ni $(OH)_2$ nanostructures for high-performance pseudocapacitor electrodes. *J. Mater. Chem. A* **2014**, *2*, 20462–20469. [CrossRef]
41. Ding, R.; Li, X.; Shi, W.; Xu, Q.; Liu, E. One-pot solvothermal synthesis of ternary Ni-Co-P micro/nano-structured materials for high performance aqueous asymmetric supercapacitors. *Chem. Eng. J.* **2017**, *320*, 376–388. [CrossRef]
42. Li, X.; Ding, R.; Shi, W.; Xu, Q.; Ying, D.; Huang, Y.; Liu, E. Hierarchical porous Co(OH)F/$Ni(OH)_2$: A new hybrid for supercapacitors. *Electrochim. Acta* **2018**, *265*, 455–473. [CrossRef]
43. Yang, S.; Wu, X.; Chen, C.; Dong, H.; Hu, W.; Wang, X. Spherical α-$Ni(OH)_2$ nanoarchitecture grown on graphene as advanced electrochemical pseudocapacitor materials. *Chem. Commun.* **2012**, *48*, 2773–2775. [CrossRef] [PubMed]
44. Zhang, J.; Chen, L.; Wang, Y.; Cai, S.; Yang, H.; Yu, H.; Ding, F.; Huang, C.; Liu, X. VO_2(B)/graphene composite-based symmetrical supercapacitor electrode via screen printing for intelligent packaging. *Nanomaterials* **2018**, *8*, 1020. [CrossRef]
45. Hwang, S.-K.; Patil, S.J.; Chodankar, N.R.; Huh, Y.S.; Han, Y.-K. An aqueous high-performance hybrid supercapacitor with MXene and polyoxometalates electrodes. *Chem. Eng. J.* **2022**, *427*, 131854. [CrossRef]
46. Karri, S.N.; Ega, S.P.; Srinivasan, P.; Perupogu, V. Used carbon water filter—A source for high performance microporous activated carbon electrode for aqueous supercapacitor. *J. Energy Storage* **2021**, *44*, 103399. [CrossRef]
47. Yang, Q.; Lu, Z.; Liu, J.; Lei, X.; Chang, Z.; Luo, L.; Sun, X. Metal oxide and hydroxide nanoarrays: Hydrothermal synthesis and applications as supercapacitors and nanocatalysts. *Prog. Nat. Sci.* **2013**, *23*, 351–366. [CrossRef]
48. Chen, X.; Wang, S.; Qiao, G.; Wang, X.; Lu, G.; Cui, H.; Wang, X. Sepiolite/amorphous nickel hydroxide hierarchical structure for high capacitive supercapacitor. *J. Alloy. Compd.* **2021**, *881*, 160519. [CrossRef]
49. Zhang, J.; Liu, Y.; Guan, H.; Zhao, Y.; Zhang, B. Decoration of nickel hydroxide nanoparticles onto polypyrrole nanotubes with enhanced electrochemical performance for supercapacitors. *J. Alloy. Compd.* **2017**, *721*, 731–740. [CrossRef]
50. Sichumsaeng, T.; Chanlek, N.; Maensiri, S. Effect of various electrolytes on the electrochemical properties of Ni $(OH)_2$ nanostructures. *Appl. Surf. Sci.* **2018**, *446*, 177–186. [CrossRef]
51. Liu, X.; Yang, Y.; Xing, X.; Wang, Z.; Wang, Y. From water and Ni foam to a $Ni(OH)_2$@Ni foam binder-free supercapacitor electrode: A green corrosion route. *ChemElectroChem* **2018**, *5*, 434–444. [CrossRef]
52. Jiao, W.; Zhang, L. Preparation and electrochemical performance of cellular structure Ni (OH) 2 thin film. *Curr. Appl. Phys.* **2016**, *16*, 115–119. [CrossRef]
53. Sichumsaeng, T.; Phromviyo, N.; Maensiri, S. Influence of gas-diffusion-layer current collector on electrochemical performance of $Ni(OH)_2$ nanostructures. *Int. J. Min. Met. Mater.* **2021**, *28*, 1038–1047. [CrossRef]
54. Liu, Y.F.; Yuan, G.H.; Jiang, Z.H.; Yao, Z.P.; Yue, M. Preparation of Ni $(OH)_2$-graphene sheet-carbon nanotube composite as electrode material for supercapacitors. *J. Alloy. Compd.* **2015**, *618*, 37–43. [CrossRef]
55. Ren, Q.; Wang, R.; Wang, H.; Key, J.; Brett, D.J.L.; Ji, S.; Yin, S.; Shen, P.K. Ranunculus flower-like $Ni(OH)_2$@ Mn_2O_3 as a high specific capacitance cathode material for alkaline supercapacitors. *J. Mater. Chem. A* **2016**, *4*, 7591–7595. [CrossRef]
56. Wang, Y.; Zhang, X.; Li, X.; Liu, Y.; Wang, X.; Liu, X.; Xu, J.; Li, Y.; Liu, Y.; Wei, H.; et al. Spontaneously grown $Ni(OH)_2$ on iron oxide nanoparticles with enhanced energy storage performance for electrodes of asymmetric supercapacitors. *RSC Adv.* **2017**, *7*, 50358–50366. [CrossRef]
57. Yu, H.; Lu, L.; Xu, T.; Zhang, T.; Yang, L.; Zhang, J.; Gu, M.; Chen, L.; Cai, T. A facile method for synthesis of $Ni(OH)_2$@xRF with excellent electrochemical performances. *Mater. Lett.* **2020**, *273*, 127867. [CrossRef]
58. Xiang, G.; Yin, J.; Qu, G.; Sun, P.; Hou, P.; Huang, J.; Xu, X. Construction of $ZnCo_2S_4$@ Ni $(OH)_2$ core–shell nanostructures for asymmetric supercapacitors with high energy densities. *Inorg. Chem. Front.* **2019**, *6*, 2135–2141. [CrossRef]